pISSN 2384-1095
eISSN 2384-1109

iMRI 2021;25:281-292

https://doi.org/10.13104/imri.2021.25.4.281

iMRI
Investigative Magnetic Resonance Imaging

Cranial Nerve Disorders: Clinical Application of High-Resolution Magnetic Resonance Imaging Techniques

Ji Ye Lee[1], Hye Min Park[1], Boeun Lee[2], Ji-hoon Kim[1]

[1]Department of Radiology, Seoul National University Hospital, Seoul National University College of Medicine, Seoul, Korea
[2]Department of Radiology, Ewha Womans University Seoul Hospital, Ewha Womans University College of Medicine, Seoul, Korea

Review Article

Received: May 27, 2021
Revised: July 2, 2021
Accepted: July 5, 2021

Correspondence to:
Ji-hoon Kim, M.D., Ph.D.
Department of Radiology, Seoul National University Hospital, Seoul National University College of Medicine, 101 Daehak-ro, Jongno-gu, Seoul 03080, Korea.
Tel. +82-2-2072-3280
Fax. +82-2-747-7418
E-mail: jihnkim@gmail.com

Cranial-nerve disorders can be caused by a wide spectrum of diseases, including congenital, inflammatory, and tumorous diseases, and are often encountered in practice. However, the imaging of cranial-nerve disorders is challenging, and understanding the anatomical differences of each region is essential for conducting the best protocols and for detecting subtle changes in cranial nerves during magnetic resonance imaging (MRI) examinations. In this review we discuss which MRI techniques are best for observing normal and pathologic appearance, according to the different regions of the cranial nerves.

Keywords: Magnetic resonance imaging; Cranial nerve; Skull base; High-resolution imaging, fluid-attenuated inversion recovery

INTRODUCTION

Cranial-nerve disorders are frequently encountered in practice and can be caused by a wide spectrum of diseases, including congenital and inflammatory diseases and tumors of the cranial nerves, or by disease propagation from the adjacent structures of the brain, skull base, or other craniofacial structures. Given its excellent soft-tissue contrast, MRI is the best imaging modality for investigating cranial-nerve disorders (1, 2). Although various methods have been used to identify cranial-nerve disorders, their imaging remains challenging because of the small caliber of cranial nerves and the complex regional anatomy (3).

With recent developments in MRI techniques, visualization of the normal anatomy of cranial nerves or their pathologic changes became feasible because of the high spatial resolution, isotropic three-dimensional imaging, and fast image acquisition of these techniques. Guided by medical history and the results of neurological examination, radiologists should set the coverage range appropriately and select optimal sequences when conducting MRI examinations for patients with suspected cranial-nerve abnormalities.

Cranial nerves comprise 12 pairs of symmetric nerves that originate from the

cerebrum and the brainstem (4). The peripheral cranial nerves consist of ten cranial nerves, from the oculomotor nerve to the hypoglossal nerve (2). Olfactory and optic nerves are direct parenchymal extensions from the telencephalon and diencephalon, respectively (5). These ten peripheral cranial nerves pass through similar anatomical structures, from the nuclei (located in the brainstem), through the skull base, and downwards to extracranial structures (2). When doing cranial-nerve-dedicated MRI examinations, one must understand the anatomical characteristics of each region in order to use the best protocols for detecting subtle changes in the cranial nerves (1, 2). In this review, we will discuss appropriate MRI techniques, focusing on various regions of the peripheral cranial nerves.

Voxel Size and Coverage

Although large cranial nerves can be partly seen even in routine MRI sequences (6, 7), few of them are usually visible with conventional MRI, because of their small caliber (4). These small structures pass through the cisternal space of the posterior fossa to the skull base, and therefore tend to be more susceptible to artifacts related to pulsation from blood vessels and cerebrospinal fluid (CSF) spaces and from the air-bone interface. Dedicated high-resolution MRI is essential to overcome these challenges (2, 4). High-resolution, thin-section imaging enables full-length tracing of the small cranial nerves. The visualization of the trochlear nerve (CN IV) is especially challenging because of its small caliber and proximity to multiple vascular structures (8). Previous studies have shown that carefully conducted high-resolution imaging (0.3 mm × 0.3 mm × 0.25 mm), with a scan plane set to an oblique axial direction perpendicular to the long axis of the cerebral aqueduct, can make the cisternal segment of the CN IV visible better than can conventional high-resolution images (0.67 mm × 0.45 mm × 1.4 mm) (9). In practice, increased spatial resolution is better for visualizing small cranial nerves, although it involves a trade-off with reduced scan coverage, decreased signal-to-noise ratio, and image degradation associated with long acquisition times (3). Therefore, image acquisition and reconstruction techniques, including parallel imaging and compressed sensing, can be applied to reduce scan time while preserving image quality (10, 11).

Multiple sub-millimetric three-dimensional isotropic images must be acquired with 0.6-mm voxels for cranial-nerve MRI (2, 4). Moreover, the scan range should be focused to cover the areas of interest chosen in terms of the patients' history and neurological signs (2). In our institution, routine high-resolution cranial-nerve imaging consists of three-dimensional heavily T2-weighted (T2W) imaging; three-dimensional contrast-enhanced T1-weighted (T1W) imaging; and non-enhanced and enhanced three-dimensional T2 fluid-attenuated inversion recovery (FLAIR) with axial and coronal reconstruction. Multiplanar reconstruction is additionally done when indicated. In selected cases, CN IV sequence or special sequences for extracranial segments of cranial nerves are added to conventional cranial-nerve protocols (9, 12).

Visualization of Normal Cranial Nerves

Cisternal and Dural Segments

Because the cisternal segment of the cranial nerve is surrounded by CSF, sub-millimetric fluid-sensitive sequences are well suited for the visualization of the cisternal positions of the cranial nerves (1, 2). High-resolution three-dimensional T2W sequences show dark cranial nerves against the background of the bright CSF and offer high resolution with a section thickness of less than 1 mm and voxel volume of less than 1 mm^3 (12-15) (Fig. 1). These sequences could be obtained by using fast gradient-echo or fast spin-echo (FSE) techniques. Fast gradient-echo sequences (true fast imaging with steady-state free precession [FISP] fast imaging employing steady-state acquisition [FIESTA], or balanced fast-field echo [b-FFE]) are typically susceptible to dephasing caused by small field inhomogeneities, resulting in banding artifacts. These artifacts could be reduced by doing two acquisitions with and without phase frequency alternations in the constructive interference into steady-state and fast imaging, employing steady-state acquisition with phase cycling sequences (constructive interference in steady state [CISS], FIESTA-C) (13). However, they typically involve longer scanning times and can be susceptible to blurring (16). One can use three-dimensional isotropic T2 fast spin-echo techniques to visualize the cisternal segment of cranial nerves, e.g., CUBE, volumetric isotropic turbo spin-echo acquisition (VISTA), or sampling perfection with application-optimized contrasts by using different flip-angle evolutions (SPACE). These approaches were developed with short, non-spatially selective radiofrequency pulses, very long echo-train length, and variable flip angles for refocusing radiofrequency pulses (suppressing blurring while reducing flow and chemical shift artifacts). These techniques enable high-resolution isotropic imaging (up to 0.3 mm)

a

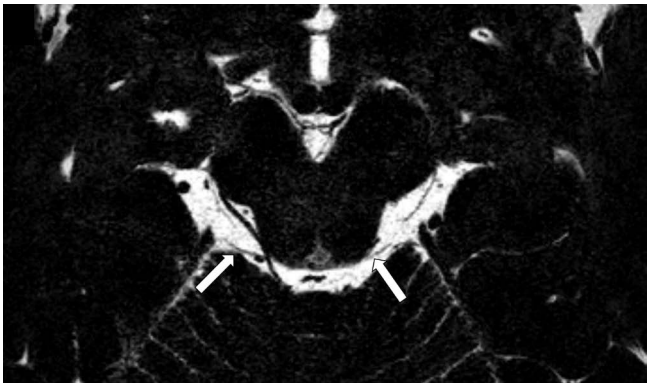

b

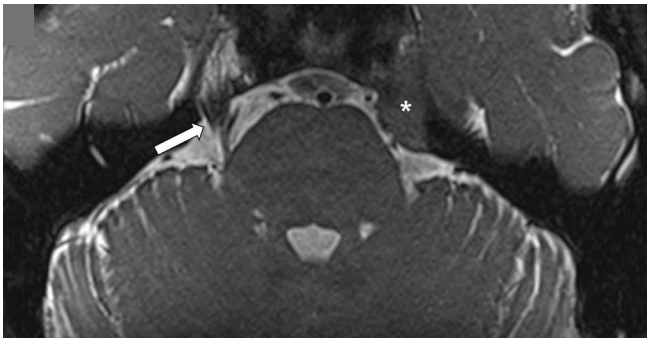

c

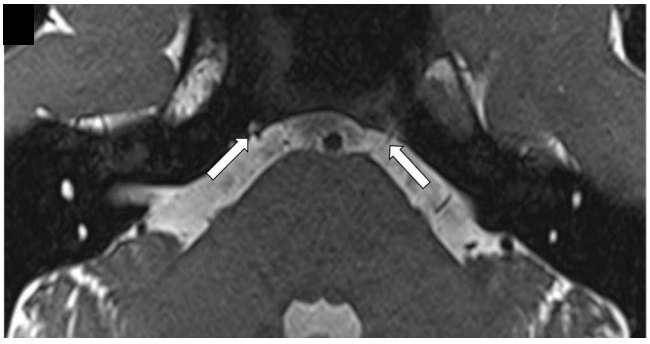

d

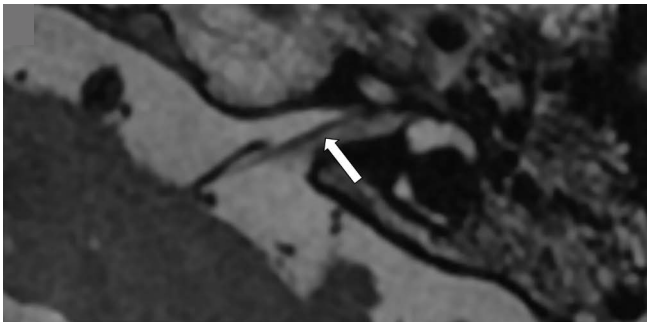

e

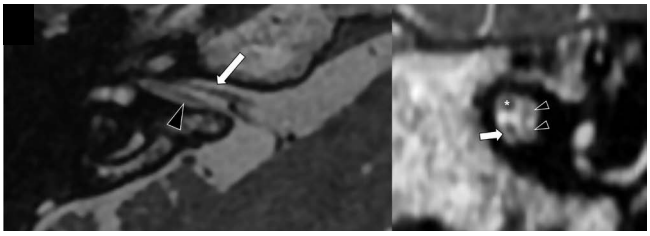

f

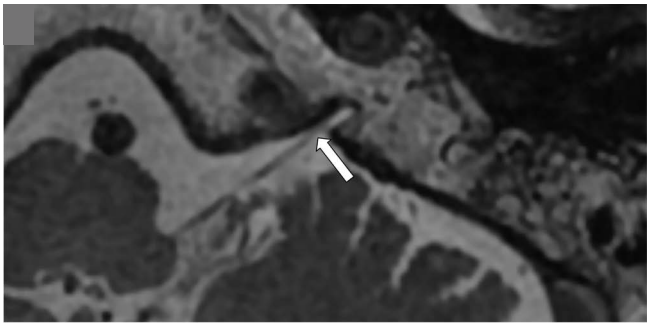

g

Fig. 1. Cranial nerves in the cisternal segment on high-resolution three-dimensional T2 weighted sequences. (a) Oculomotor nerves (white arrows). (b) Trochlear nerves (white arrows). (c) Trigeminal nerve (white arrow), a meningioma in the left Meckel's cave (asterisk). (d) Abducens nerves entering the Dorello's canal (white arrows). (e) Facial nerve (white arrow). (f) Vestibulocochlear nerve on axial (left) and oblique sagittal reconstruction image (right), cochlear nerve (white arrows), vestibular nerves (black arrowheads), facial nerve (asterisk). (g) Glossopharyngeal nerve (white arrow).

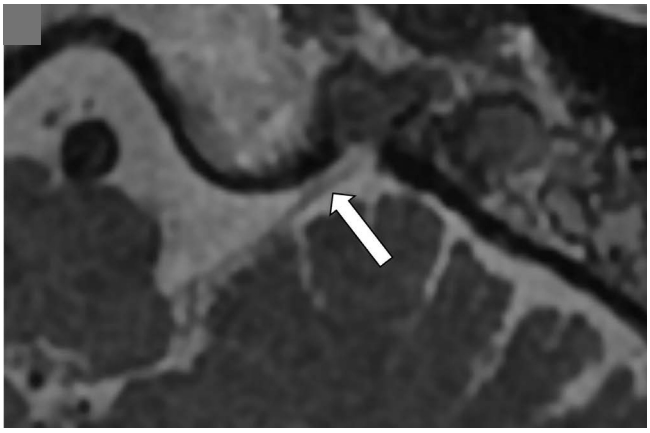

h

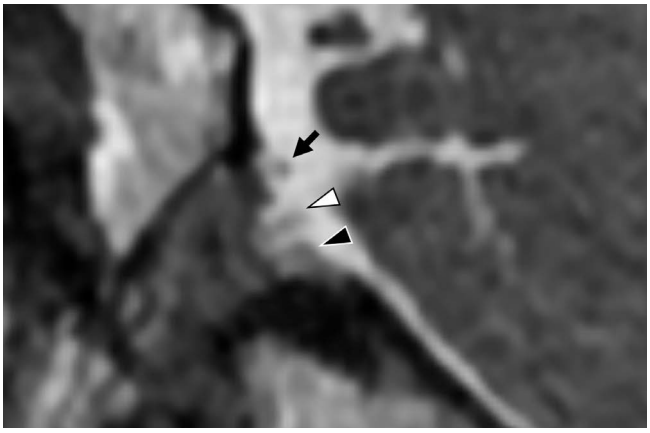

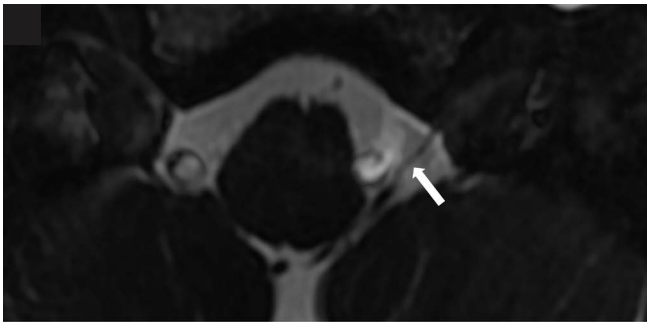

i

Fig. 1. (h) Vagus and spinal accessory nerves (left, axial; right, oblique sagittal), vagus nerve-spinal accessory nerve complex (white arrow on axial), glossopharyngeal nerve (black arrow), vagus nerve (white arrowhead), and spinal accessory nerve (black arrowhead). (i) Hypoglossal nerve (white arrow).

with a high contrast-to-noise ratio (17, 18). These three-dimensional T2W images have become routine in otologic imaging for demonstrating labyrinthine anomalies (19, 20), detection or differentiation of labyrinthitis ossificans (21), intralabyrinthine schwannomas (22), or the preoperative work-up of cochlear implantation (to evaluate the size of the cochlear nerve and cochlea as well as the patency of the cochlear aperture) (23, 24). High-resolution cisternographic images are the modality of choice in neurovascular compression, enabling vascular contact in the transition zone. Three-dimensional data offer benefits for multiplanar reconstruction in visualizing the culprit vessel by showing the full course of the transition zones of various cranial nerves (25-28). Because three-dimensional T2W images provide the highest resolution among three-dimensional imaging sequences, this sequence is the modality of choice for patients with congenital trochlear nerve palsy in order to detect congenital aplasia or hypoplasia of the trochlear nerve (29, 30).

Interdural and Foraminal Segments

The dura mater consists of two layers, the outer periosteal layer and the inner meningeal or cerebral layer. The outer layer adheres to the inner table of the skull and is continuous with the outer periosteum through sutures and the foramina. The inner layer is usually fused with the outer layer; however, there are interdural spaces in which these two layers are not fused, such as in regions with dural venous sinuses (1, 2). The cavernous sinus and petroclival venous plexus are examples of the interdural spaces.

Except for the vestibulocochlear nerve, most of the cranial nerves exit the cranium and run into extracranial structures via the skull-base foramina. The foraminal segment of a cranial nerve is defined from the inner margin of the internal orifice of the skull-base foramen to the outer margin of the outer table at the external orifice. Because the cranial nerve and abundant circumneural venous plexus exist in the foraminal segment of cranial nerves, normal nerves appear as non-enhanced filling-defect-like structures, surrounded by the prominently enhancing venous plexus on MRI (31) (Fig. 2). Therefore, three-dimensional high-resolution contrast-enhanced T1W images could be used to visualize normal cranial nerves in the interdural or foraminal segment. The mainstay of three-dimensional

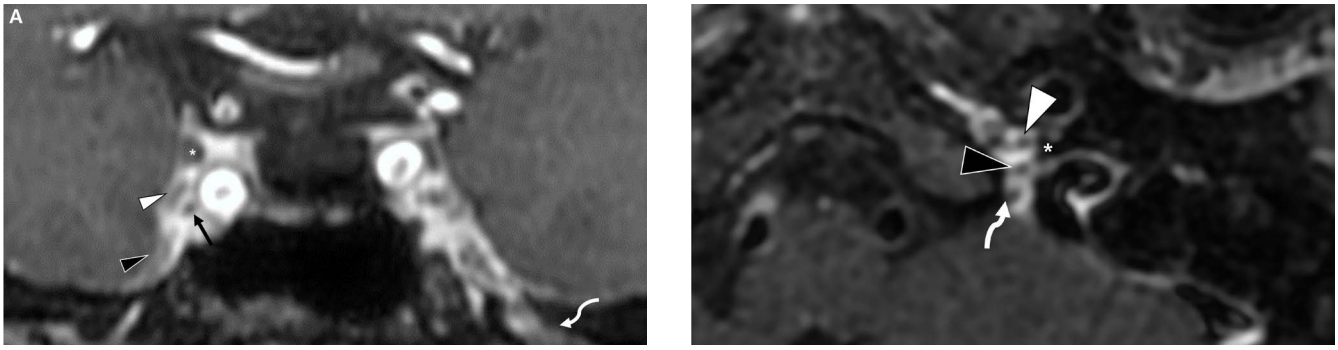

Fig. 2. Cranial nerves in the foraminal and interdural segments on high-resolution contrast-enhanced T1 weighted sequences. (a) Cranial nerves within the cavernous sinus, oculomotor nerve (asterisk), ophthalmic nerve (white arrowhead), maxillary nerve (black arrowhead), mandibular nerve (curved white arrow), and abducens nerve (black arrow). (b) Lower cranial nerves at the jugular foramen, glossopharyngeal nerve (white arrowhead), vagus nerve (black arrowhead), spinal accessory nerve (curved white arrow), jugular spine (asterisk).

sequences consists of ultrafast spoiled GE sequences with small flip angles and short repetition times (1). Isotropic data offer various benefits for multiplanar reconstruction in the complex skull base (32). The sequences for acquiring these data typically have pre-pulses (magnetization preparation) to provide T1W and T2W or fat suppression and can be combined with partial k-space sampling to further reduce acquisition times. Examples include volumetric interpolated breath-hold examination (VIBE) from Siemens and T1W as well as high-resolution isotropic volume examination from Philips (33). Special FSE sequences, such as VISTA and SPACE, can be used as alternatives to fast GE sequences to produce high-resolution fat-suppressed T1W imaging (34). They are also resistant to susceptibility artifacts, which is a useful characteristic at the skull base. Another advantage of these sequences arises from their inherent flow suppression caused by the dephasing of flowing spins, which can prevent vascular time-of-flight effects from simulating lesions at the skull base (35).

Mixed-weighting steady-state free precession (SSFP) or reversed fast imaging with steady-state precession (PSIF) and contrast administration can be also used to visualize nerves in the foraminal segments with the advent of high spatial resolution and T1 shortening effect after contrast administration. Normal cranial nerves can be well visualized inside the cavernous sinus, surrounded by bright contrast-enhanced venous blood (36). However, gadolinium-enhanced T1-weighted sequences have limitations for distinguishing pathologic from normal enhancement in some cranial nerves in the interdural or foraminal segments, including the trigeminal ganglion within the Meckel's cave (2, 37) and the geniculate, tympanic, or mastoid segment of the facial nerve (38, 39).

Extraforaminal Segment

The extraforaminal segment includes parts starting from the outer cortex of the outer margin of the skull-base foramen (1, 2). The cranial nerve passes through different types of soft tissue, including fat, vessels, glands, muscles, and viscera, until it reaches its final destination (1). The normal extraforaminal cranial nerve could appear as a hypointense tubular structure within hyperintense fatty tissue on high-resolution T1WI without fat suppression (2). However, for detecting pathologic signal changes of enhancement of the cranial nerves, fat suppression is mandatory to maximize the tissue contrast between the suppressed fatty tissue and the hyperintense nerve (2). Sequences such as CISS and FIESTA, which are fully refocused (balanced) steady-state sequences that demonstrate both T2 and T1 components, could help the differentiation of nerves with high resolution from tissues having various properties (1). Specifically, several reports have shown the value of special high-resolution sequences for extracranial cranial-nerve imaging, such as three-dimensional PSIF with diffusion-weighted imaging (DWI) or three-dimensional double echo steady-state with water excitation (3D DESS-WE). The DESS sequence involves the acquisition of two different echoes: the gradient echo used in the FISP sequence and spin echo used in the PSIF sequence. The PSIF signal accentuates the signal intensities of components with long T2, whereas the FISP signal intensity provides more anatomic details with a contrast

dominated by the T1/T2 ratio. In the WE technique, only water is excited by using section-selective composite pulses, thus avoiding disruptions of the steady state and ensuring uniform fat suppression. When DESS is combined with WE, the facial nerve is clearly shown without relying on the fatty-tissue background. The DESS-WE sequences also demonstrate flow sensitivity, because of which stationary fluids (such as saliva in parotid ducts) show high signal intensity with suppressed carotid artery flow. This technique works well for visualizing the intraparotid facial nerve and extracranial trigeminal nerve (40-42) (Figs. 3, 4).

The advantages of three-dimensional PSIF-DWI arise from its dominant T2 contrast of reversed FISP and the accentuation of anisotropic diffusion characteristics of peripheral nerves in combination with DWI (43, 44). The use of three-dimensional PSIF-DWI could achieve excellent nerve-muscle contrast with blood suppression and simultaneously display the intraparotid facial nerve and parotid duct with excellent soft-tissue contrast.

Imaging of Pathologic Signals of Cranial Nerves

Traditionally, gadolinium-enhanced T1W spin-echo and three-dimensional gradient echo sequences were used to evaluate the pathologic enhancement in cranial nerves. However, because of the presence of the circumneural venous plexus, these techniques have shown significant limitations by inhibiting the evaluation of the real pathologic enhancement of the nerve caused by inflammatory or neoplastic breakdown of the blood-nerve barrier (38, 39, 45).

In the last decade, isotopic three-dimensional T2W FLAIR, using three-dimensional turbo spin-echo sequences with

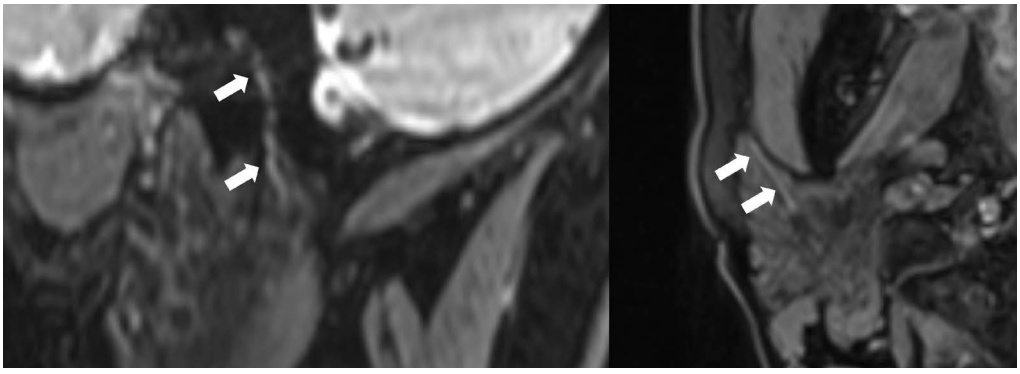

Fig. 3. Extraforaminal segment of facial nerve on double-echo steady-state sequence with water excitation (DESS-WE) sequence (left, sagittal; right, axial, arrows).

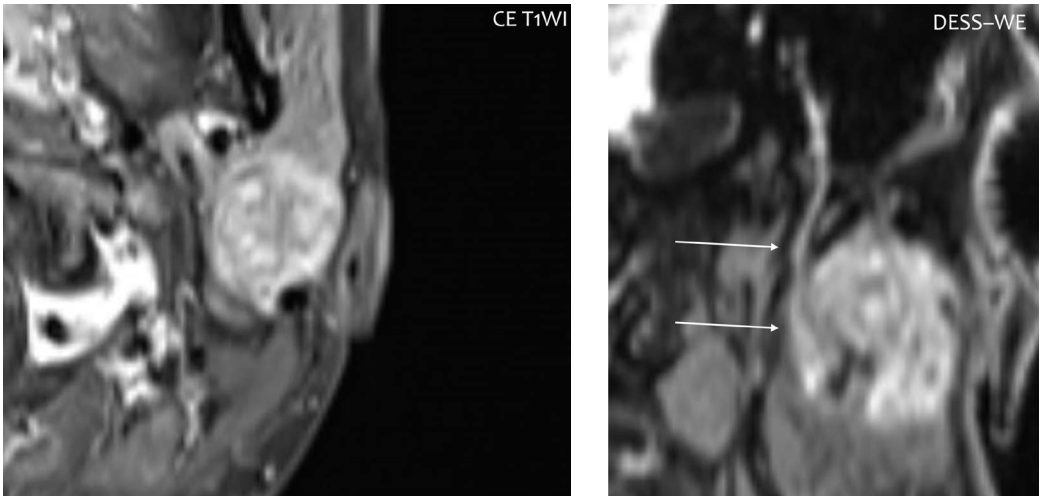

Fig. 4. A 35-year-old patient with a mucoepidermoid carcinoma in the left parotid gland. A double-echo steady-state sequence with water excitation (DESS-WE) sequence with coronal reconstruction shows the relationship between the main trunk of the facial nerve (thin arrows) and the tumor.

variable flip angles (VISTA, SPACE, or CUBE), was introduced on the 3T MR system (34). This sequence uses variable refocusing flip angles to constrain T2 decay over a long echo train with minimal blurring and can acquire isotropic resolutions in a clinically acceptable scan time. This ability of the three-dimensional high-resolution FLAIR sequence to find minute abnormalities mainly results from FLAIR imaging's high sensitivity to subtle changes in longitudinal magnetization in the fluid space. This sensitivity declines with increasing concentration of the contrast agent in a manner that is different from that of other T1W images (46, 47). The three-dimensional-FLAIR sequence also suppresses the signal intensity from the fluid flowing at a velocity exceeding 1.0 cm/s (48). Three-dimensional FLAIR sequences provide exquisite CSF suppression with fewer CSF-related flow artifacts in the posterior fossa, while enabling visualization of the T2 prolongation of the affected lesion (49, 50) (Figs. 5-7). Previous studies have shown the advantage of three-dimensional FLAIR sequences for detecting pathologic signal alterations and abnormal enhancement of the nerve itself, which could be beneficial for the diagnosis of various cranial-nerve pathologies, including facial neuritis (51), vestibular neuritis (52, 53), Ramsay-Hunt syndrome (54), and antiGQ1b antibody syndrome (55). The role of high-resolution three-dimensional FLAIR imaging has also been highlighted in otologic imaging to detect abnormal labyrinthine signal changes in the onset of sudden sensorineural hearing loss (56-59) and *in vivo* imaging of endolymphatic hydrops (60-62). Table 1 summarizes the indications and representative sequences of cranial-nerve MRI.

Recent Advances in Cranial-Nerve Imaging

Cranial-nerve imaging requires a relatively long scan time to render small cranial nerves visible, and these are often

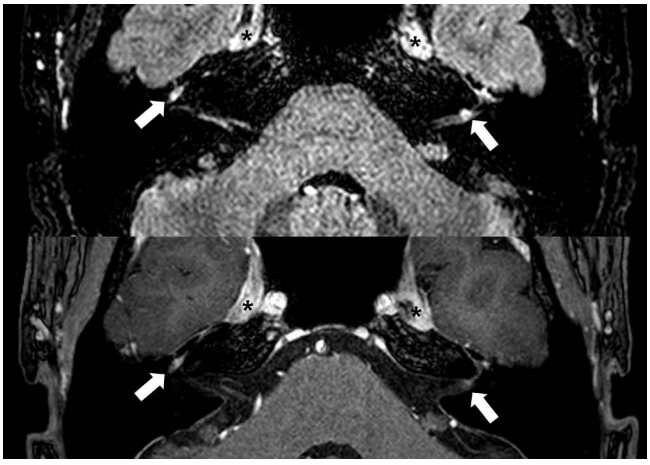

Fig. 5. A 50-year-old patient with chronic inflammatory demyelinating polyneuropathy. Bilateral facial nerves show contrast enhancement, which is more visible on contrast-enhanced fluid attenuated inversion recovery (FLAIR) (arrows in the upper row) than on a contrast-enhanced T1 weighted image (arrows in the lower row). Thickened and enhanced trigeminal nerves (black asterisks).

a b c

Fig. 6. A 57-year-old woman with anti-GQ1b antibody syndrome, presenting with diplopia, areflexia, and ataxia. Precontrast three-dimensional fluid attenuated inversion recovery (FLAIR) image (a) shows mild hyperintensity of both oculomotor nerves (arrows). Post three-dimensional FLAIR image (b) shows multifocal enhancement of the left oculomotor nerve (arrow) including the neuromuscular junction (arrowhead). Three-dimensional CE T1- turbo field echo (TFE) (c) shows long segmental enhancement of both oculomotor nerve (arrows).

Table 1. Recommended Pulse Sequences for Cranial Nerve MRI according to Clinical Situation and Cranial Nerve Segments

	Cranial nerve segment	Pulse sequences	Representative product sequences
Anatomy	Cisternal/dural cave segment	3D heavily T2-weighted fast gradient echo	3D fully refocussed (balanced) steady-state free precession:
			– TrueFISP (Siemens), FIESTA (GE), bFFE (Philips)
			MIP of TrueFISP sequences of alternating and non-alternating RF pulses:
			– CISS (Siemens), FIESTA-C (GE)
		3D heavily T2-weighted fast spin echo	Rapid recovery of longitudinal magnetization through a 90 degree RF pulse at the end of the echo train (driven equilibrium):
			– RESTORE (Siemens), FRFSE (fast recovery fast spin echo, GE), DRIVE (Philips)
			Special 3D FSE techniques
			– SPACE (Siemens), CUBE (GE), VISTA (Philips)
	Interdural/foraminal segment	3D contrast-enhanced T1-weighted fast gradient echo	bTFE (Philips), MPRAGE (Siemens), FSPGR (GE), THRIVE (Philips), VIBE (Siemens)
		3D contrast-enhanced balanced SSFP	bFFE (Philips), CISS (Siemens), FIESTA (GE)
	Extraforaminal	T1-weighted spin echo	bFFE (Philips), CISS (Siemens), FIESTA (GE), PSIF-DWI (Philips)
		3D balanced SSFP with/without contrast enhancement	DESS-WE (Siemens)
		3D reversed FISP	
Pathology	Interdural/foraminal segment	3D contrast-enhanced balanced SSFP	bFFE (Philips), CISS (Siemens), FIESTA (GE),
	All segments	3D contrast-enhanced T1-weighted fast gradient echo	bTFE (Philips), MPRAGE (Siemens), FSPGR (GE), THRIVE (Philips), VIBE (Siemens)
	All segments	3D FLAIR with/without contrast enhancement	SPACE (Siemens), CUBE (GE), VISTA (Philips)

2D = two-dimensional; 3D = three-dimensional; bFFE = balanced fast field echo; bTFE = balanced turbo field echo; CISS = constructive interference in steady state; DESS-WE = double-echo steady-state with water excitation; DRIVE = driven equilibrium radiofrequency reset pulse; FIESTA = fast imaging employing steady state acquisition; FISP = fast imaging with steady-state free precession; FRFSE = fast recovery fast spin-echo; FSPGR =fast spoiled gradient echo; m-FFE = Multi-echo fast field echo; MPRAGE = magnetization-prepared rapid gradient echo; PSIF-DWI = reversed FISP with diffusion weighted imaging; SPACE = sampling perfection with application-optimized contrasts by using different flip angle evolutions; SSFP = steady-state free precession; THRIVE = T1-weighted high resolution isotropic volume examination; VIBE = volumetric interpolated breath-hold examination; VISTA = volumetric isotropic turbo spin echo acquisition

accompanied by motion artifacts associated with long scan time (3). Recent imaging techniques, including parallel imaging and compressed sensing (CS), have been introduced to reduce the scan time while preserving acceptable image quality (11). Conventional parallel-imaging techniques, such as sensitivity encoding (SENSE) and generalized autocalibrating partial-parallel acquisition (GRAPPA), have been widely used in cranial-nerve imaging. However, these have had limitations in reducing scan time and having a good image quality/scan range (63, 64). CS is a recently introduced technique in MR imaging, characterized by non-uniform sampling of k-space, iterative reconstruction, and reduced scan time (65-67). A recently published study has shown the benefit of combining parallel imaging and CS (such as in SENSE-CS) in patients with suspected neurovascular compression to reduce scan time yet have acceptable image quality (10).

In conclusion, recent advances in MRI technology have enabled anatomical imaging of small cranial nerves that could not have been seen on conventional brain MR imaging. In this review, we have described the best MRI techniques for observing normal and pathologic changes in the cranial nerves for different regions of the cranial nerves. Radiologists should be familiar with the normal anatomy and basic sequences for cranial-nerve imaging in order to guide optimized imaging, which will eventually lead to improved patient management.

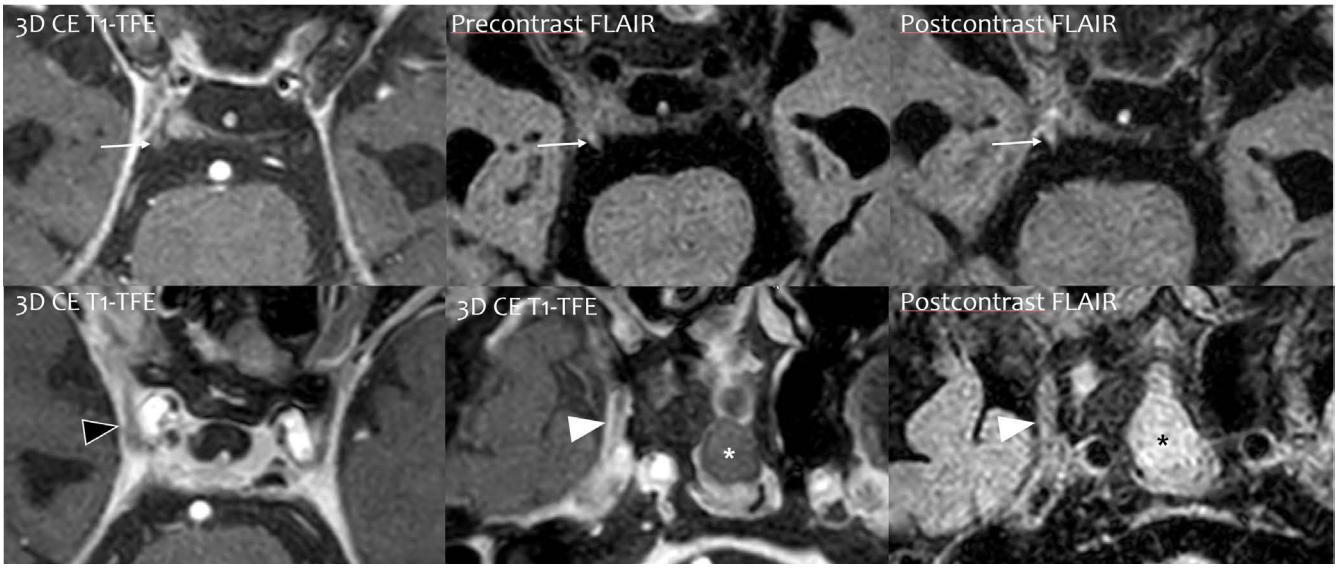

Fig. 7. A 84-year-old woman with invasive fungal sinusitis, with headache, fever, and diplopia. Postcontrast three-dimensional fluid attenuated inversion recovery (FLAIR) shows prominent enhancement of the right abducens nerve (thin arrows) when it enters the Dorello's canal, whereas three-dimensional CE-T1 turbo field echo (TFE) and precontrast FLAIR show equivocal findings (upper row). High-resolution images show the thickening and enhancement of the right oculomotor (black arrowhead) and maxillary nerves (white arrowheads) (asterisks, fungal ball in the left sphenoid sinus, lower row).

REFERENCES

1. Blitz AM, Choudhri AF, Chonka ZD, et al. Anatomic considerations, nomenclature, and advanced cross-sectional imaging techniques for visualization of the cranial nerve segments by MR imaging. Neuroimaging Clin N Am 2014;24:1-15
2. Casselman J, Mermuys K, Delanote J, Ghekiere J, Coenegrachts K. MRI of the cranial nerves--more than meets the eye: technical considerations and advanced anatomy. Neuroimaging Clin N Am 2008;18:197-231, preceding x
3. Zaitsev M, Maclaren J, Herbst M. Motion artifacts in MRI: a complex problem with many partial solutions. J Magn Reson Imaging 2015;42:887-901
4. Romano N, Federici M, Castaldi A. Imaging of cranial nerves: a pictorial overview. Insights Imaging 2019;10:33
5. Kim HJ, Seong M, Kim Y. Normal anatomy of cranial nerves III-XII on magnetic resonance imaging. J Korean Soc Radiol 2020;81:501-529
6. Kim TK, Kim HY, Yu IK, Son H-j, Chang DS, Jang YD. Schwannoma of the tongue base with imaging features and differential diagnosis: a rare case report and literature review. Investig Magn Reson Imaging 2019;23:385-389
7. Seo M, Choi Y, Lee S, et al. Diagnostic value of susceptibility-weighted MRI in differentiating cerebellopontine angle schwannoma from meningioma. Investig Magn Reson Imaging 2020;24:38-45
8. Yousry I, Camelio S, Schmid UD, et al. Visualization of cranial nerves I-XII: value of 3D CISS and T2-weighted FSE sequences. Eur Radiol 2000;10:1061-1067
9. Choi BS, Kim JH, Jung C, Hwang JM. High-resolution 3D MR imaging of the trochlear nerve. AJNR Am J Neuroradiol 2010;31:1076-1079
10. Cho SJ, Choi YJ, Chung SR, Lee JH, Baek JH. High-resolution MRI using compressed sensing-sensitivity encoding (CS-SENSE) for patients with suspected neurovascular compression syndrome: comparison with the conventional SENSE parallel acquisition technique. Clin Radiol 2019;74:817 e819-817 e814
11. Tsao J, Kozerke S. MRI temporal acceleration techniques. J Magn Reson Imaging 2012;36:543-560
12. Moon WJ, Roh HG, Chung EC. Detailed MR imaging anatomy of the cisternal segments of the glossopharyngeal, vagus, and spinal accessory nerves in the posterior fossa: the use of 3D balanced fast-field echo MR imaging. AJNR Am J Neuroradiol 2009;30:1116-1120
13. Chavhan GB, Babyn PS, Jankharia BG, Cheng HL, Shroff MM. Steady-state MR imaging sequences: physics, classification, and clinical applications. Radiographics 2008;28:1147-1160
14. Ciftci E, Anik Y, Arslan A, Akansel G, Sarisoy T, Demirci A.

Driven equilibrium (drive) MR imaging of the cranial nerves V-VIII: comparison with the T2-weighted 3D TSE sequence. Eur J Radiol 2004;51:234-240
15. Sheth S, Branstetter BF 4th, Escott EJ. Appearance of normal cranial nerves on steady-state free precession MR images. Radiographics 2009;29:1045-1055
16. Touska P, Connor SEJ. Recent advances in MRI of the head and neck, skull base and cranial nerves: new and evolving sequences, analyses and clinical applications. Br J Radiol 2019;92:20190513
17. Kojima S, Suzuki K, Hirata M, Shinohara H, Ueno E. Depicting the semicircular canals with inner-ear MRI: a comparison of the SPACE and TrueFISP sequences. J Magn Reson Imaging 2013;37:652-659
18. Lane JI, Witte RJ, Bolster B, Bernstein MA, Johnson K, Morris J. State of the art: 3T imaging of the membranous labyrinth. AJNR Am J Neuroradiol 2008;29:1436-1440
19. Connor SEJ, Dudau C, Pai I, Gaganasiou M. Is CT or MRI the optimal imaging investigation for the diagnosis of large vestibular aqueduct syndrome and large endolymphatic sac anomaly? Eur Arch Otorhinolaryngol 2019;276:693-702
20. Reinshagen KL, Curtin HD, Quesnel AM, Juliano AF. Measurement for detection of incomplete partition type II anomalies on MR imaging. AJNR Am J Neuroradiol 2017;38:2003-2007
21. Isaacson B, Booth T, Kutz JW Jr, Lee KH, Roland PS. Labyrinthitis ossificans: how accurate is MRI in predicting cochlear obstruction? Otolaryngol Head Neck Surg 2009;140:692-696
22. Salzman KL, Childs AM, Davidson HC, Kennedy RJ, Shelton C, Harnsberger HR. Intralabyrinthine schwannomas: imaging diagnosis and classification. AJNR Am J Neuroradiol 2012;33:104-109
23. Tamplen M, Schwalje A, Lustig L, Alemi AS, Miller ME. Utility of preoperative computed tomography and magnetic resonance imaging in adult and pediatric cochlear implant candidates. Laryngoscope 2016;126:1440-1445
24. Walton J, Gibson WP, Sanli H, Prelog K. Predicting cochlear implant outcomes in children with auditory neuropathy. Otol Neurotol 2008;29:302-309
25. Haller S, Etienne L, Kovari E, Varoquaux AD, Urbach H, Becker M. Imaging of neurovascular compression syndromes: trigeminal neuralgia, hemifacial spasm, vestibular paroxysmia, and glossopharyngeal neuralgia. AJNR Am J Neuroradiol 2016;37:1384-1392
26. Hughes MA, Branstetter BF, Taylor CT, et al. MRI findings in patients with a history of failed prior microvascular decompression for hemifacial spasm: how to image and where to look. AJNR Am J Neuroradiol 2015;36:768-773
27. Hughes MA, Frederickson AM, Branstetter BF, Zhu X, Sekula RF Jr. MRI of the trigeminal nerve in patients with trigeminal neuralgia secondary to vascular compression. AJR Am J Roentgenol 2016;206:595-600
28. Sivarasan N, Touska P, Murdin L, Connor S. MRI findings in vestibular paroxysmia - an observational study. J Vestib Res 2019;29:137-145
29. Holmes JM, Mutyala S, Maus TL, Grill R, Hodge DO, Gray DT. Pediatric third, fourth, and sixth nerve palsies: a population-based study. Am J Ophthalmol 1999;127:388-392
30. Kim JH, Hwang JM. Usefulness of MR imaging in children without characteristic clinical findings of Duane's retraction syndrome. AJNR Am J Neuroradiol 2005;26:702-705
31. Williams LS, Schmalfuss IM, Sistrom CL, et al. MR imaging of the trigeminal ganglion, nerve, and the perineural vascular plexus: normal appearance and variants with correlation to cadaver specimens. AJNR Am J Neuroradiol 2003;24:1317-1323
32. Barkhof F, Pouwels PJ, Wattjes MP. The Holy Grail in diagnostic neuroradiology: 3T or 3D? Eur Radiol 2011;21:449-456
33. Ahn SS, Kim J, An C, et al. Preoperative imaging evaluation of head and neck cancer: comparison of 2D spin-echo and 3D THRIVE MRI techniques with resected tumours. Clin Radiol 2012;67:e98-e104
34. Mugler JP 3rd. Optimized three-dimensional fast-spin-echo MRI. J Magn Reson Imaging 2014;39:745-767
35. Kato Y, Higano S, Tamura H, et al. Usefulness of contrast-enhanced T1-weighted sampling perfection with application-optimized contrasts by using different flip angle evolutions in detection of small brain metastasis at 3T MR imaging: comparison with magnetization-prepared rapid acquisition of gradient echo imaging. AJNR Am J Neuroradiol 2009;30:923-929
36. Yagi A, Sato N, Taketomi A, et al. Normal cranial nerves in the cavernous sinuses: contrast-enhanced three-dimensional constructive interference in the steady state MR imaging. AJNR Am J Neuroradiol 2005;26:946-950
37. Blitz AM, Macedo LL, Chonka ZD, et al. High-resolution CISS MR imaging with and without contrast for evaluation of the upper cranial nerves: segmental anatomy and selected pathologic conditions of the cisternal through extraforaminal segments. Neuroimaging Clin N Am 2014;24:17-34
38. Hong HS, Yi BH, Cha JG, et al. Enhancement pattern of the normal facial nerve at 3.0 T temporal MRI. Br J Radiol 2010;83:118-121
39. Kinoshita T, Ishii K, Okitsu T, Okudera T, Ogawa T. Facial nerve palsy: evaluation by contrast-enhanced MR imaging.

Clin Radiol 2001;56:926-932
40. Fujii H, Fujita A, Kanazawa H, Sung E, Sakai O, Sugimoto H. Localization of parotid gland tumors in relation to the intraparotid facial nerve on 3D double-echo steady-state with water excitation sequence. AJNR Am J Neuroradiol 2019;40:1037-1042
41. Fujii H, Fujita A, Yang A, et al. Visualization of the peripheral branches of the mandibular division of the trigeminal nerve on 3D double-echo steady-state with water excitation sequence. AJNR Am J Neuroradiol 2015;36:1333-1337
42. Qin Y, Zhang J, Li P, Wang Y. 3D double-echo steady-state with water excitation MR imaging of the intraparotid facial nerve at 1.5T: a pilot study. AJNR Am J Neuroradiol 2011;32:1167-1172
43. Chu J, Zhou Z, Hong G, et al. High-resolution MRI of the intraparotid facial nerve based on a microsurface coil and a 3D reversed fast imaging with steady-state precession DWI sequence at 3T. AJNR Am J Neuroradiol 2013;34:1643-1648
44. Naganawa S, Ishihara S, Satake H, Kawai H, Sone M, Nakashima T. Simultaneous three-dimensional visualization of the intra-parotid facial nerve and parotid duct using a three-dimensional reversed FISP sequence with diffusion weighting. Magn Reson Med Sci 2010;9:153-158
45. Gebarski SS, Telian SA, Niparko JK. Enhancement along the normal facial nerve in the facial canal: MR imaging and anatomic correlation. Radiology 1992;183:391-394
46. Deliganis AV, Fisher DJ, Lam AM, Maravilla KR. Cerebrospinal fluid signal intensity increase on FLAIR MR images in patients under general anesthesia: the role of supplemental O2. Radiology 2001;218:152-156
47. Maeda M, Tsuchida C. "Ivy sign" on fluid-attenuated inversion-recovery images in childhood moyamoya disease. AJNR Am J Neuroradiol 1999;20:1836-1838
48. Fukuoka H, Hirai T, Okuda T, et al. Comparison of the added value of contrast-enhanced 3D fluid-attenuated inversion recovery and magnetization-prepared rapid acquisition of gradient echo sequences in relation to conventional postcontrast T1-weighted images for the evaluation of leptomeningeal diseases at 3T. AJNR Am J Neuroradiol 2010;31:868-873
49. Kallmes DF, Hui FK, Mugler JP 3rd. Suppression of cerebrospinal fluid and blood flow artifacts in FLAIR MR imaging with a single-slab three-dimensional pulse sequence: initial experience. Radiology 2001;221:251-255
50. Naganawa S, Koshikawa T, Nakamura T, et al. Comparison of flow artifacts between 2D-FLAIR and 3D-FLAIR sequences at 3 T. Eur Radiol 2004;14:1901-1908
51. Lim HK, Lee JH, Hyun D, et al. MR diagnosis of facial neuritis: diagnostic performance of contrast-enhanced 3D-FLAIR technique compared with contrast-enhanced 3D-T1-fast-field echo with fat suppression. AJNR Am J Neuroradiol 2012;33:779-783
52. Byun H, Chung JH, Lee SH, Park CW, Park DW, Kim TY. Clinical value of 4-hour delayed gadolinium-enhanced 3D FLAIR MR images in acute vestibular neuritis. Laryngoscope 2018;128:1946-1951
53. Venkatasamy A, Huynh TT, Wohlhuter N, et al. Superior vestibular neuritis: improved detection using FLAIR sequence with delayed enhancement (1 h). Eur Arch Otorhinolaryngol 2019;276:3309-3316
54. Chung MS, Lee JH, Kim DY, et al. The clinical significance of findings obtained on 3D-FLAIR MR imaging in patients with Ramsay-Hunt syndrome. Laryngoscope 2015;125:950-955
55. Lee B, Lee JH, Lim YM, et al. High-resolution MR imaging of cranial neuropathy in patients with anti-GQ1b antibody syndrome. J Neurol Sci 2021;423:117380
56. Eliezer M, Maquet C, Horion J, et al. Detection of intralabyrinthine abnormalities using post-contrast delayed 3D-FLAIR MRI sequences in patients with acute vestibular syndrome. Eur Radiol 2019;29:2760-2769
57. Lee JW, Park YA, Park SM, et al. Clinical features and prognosis of sudden sensorineural hearing loss secondary to intralabyrinthine hemorrhage. J Audiol Otol 2016;20:31-35
58. Gao Z, Chi FL. The clinical value of three-dimensional fluid-attenuated inversion recovery magnetic resonance imaging in patients with idiopathic sudden sensorineural hearing loss: a meta-analysis. Otol Neurotol 2014;35:1730-1735
59. Naganawa S, Kawai H, Taoka T, et al. Heavily T(2)-weighted 3D-FLAIR improves the detection of cochlear lymph fluid signal abnormalities in patients with sudden sensorineural hearing loss. Magn Reson Med Sci 2016;15:203-211
60. Attye A, Eliezer M, Boudiaf N, et al. MRI of endolymphatic hydrops in patients with Meniere's disease: a case-controlled study with a simplified classification based on saccular morphology. Eur Radiol 2017;27:3138-3146
61. Nakashima T, Naganawa S, Sugiura M, et al. Visualization of endolymphatic hydrops in patients with Meniere's disease. Laryngoscope 2007;117:415-420
62. Barath K, Schuknecht B, Naldi AM, Schrepfer T, Bockisch CJ, Hegemann SC. Detection and grading of endolymphatic hydrops in Meniere disease using MR imaging. AJNR Am J Neuroradiol 2014;35:1387-1392
63. Aja-Fernandez S, Vegas-Sanchez-Ferrero G, Tristan-Vega A. Noise estimation in parallel MRI: GRAPPA and SENSE. Magn Reson Imaging 2014;32:281-290
64. Petr J, Kybic J, Bock M, Muller S, Hlavac V. Parallel image

reconstruction using B-spline approximation (PROBER). Magn Reson Med 2007;58:582-591
65. Suh CH, Jung SC, Lee HB, Cho SJ. High-resolution magnetic resonance imaging using compressed sensing for intracranial and extracranial arteries: comparison with conventional parallel imaging. Korean J Radiol 2019;20:487-497
66. Toledano-Massiah S, Sayadi A, de Boer R, et al. Accuracy of the compressed sensing accelerated 3D-FLAIR sequence for the detection of MS plaques at 3T. AJNR Am J Neuroradiol 2018;39:454-458
67. Eichinger P, Hock A, Schon S, et al. Acceleration of double inversion recovery sequences in multiple sclerosis with compressed sensing. Invest Radiol 2019;54:319-324